JOM, Vol. 69, No. 8, 2017
DOI: 10.1007/s11837-017-2319-5
© 2017 The Minerals, Metals & Materials Society

Effect of Grain Orientation and Boundary Distributions on Hydrogen-Induced Cracking in Low-Carbon-Content Steels

MOHAMMAD MASOUMI,[1,2,4] HANA LIVIA FROTA COELHO,[1] SÉRGIO SOUTO MAIOR TAVARES,[3] CLEITON CARVALHO SILVA,[1] and HAMILTON FERREIRA GOMES DE ABREU[1]

1.—Departamento de Engenharia Metalúrgica e de Materiais, Centro de Tecnologia, Universidade Federal do Ceará, Fortaleza, CE CEP 60455-760, Brazil. 2.—Escola Politécnica da Universidade de São Paulo, São Paulo, SP CEP 05508-900, Brazil. 3.—Departamento de Engenharia Mecânica/PGMEC, Universidade Federal Fluminense, Niterói, RJ CEP 24210-240, Brazil. 4.—e-mail: mohammad@alu.ufc.br

Hydrogen-induced cracking (HIC) causes considerable economic losses in a wide range of steels exposed to corrosive environments. The effect of crystallographic texture and grain boundary distributions tailored by rolling at 850 °C in three different steels with a body-centered cube structure was investigated on HIC resistance. The x-ray and electron backscattered diffraction techniques were used to characterize texture evolutions during the rolling process. The findings revealed a significant improvement against HIC based on texture engineering. In addition, increasing the number of {111} and {110} grains, associated with minimizing the number of {001} grains in warm-rolled samples, reduced HIC susceptibility. Moreover, the results showed that boundaries associated with low {hkl} indexing and denser packing planes had more resistance against crack propagation.

INTRODUCTION

Hydrogen-induced cracking (HIC), the progressive nucleation and crack propagation along metallurgical defects such as inclusions, precipitations, phase interfaces, martensite islands, and grain boundaries, causes considerable economic losses in the petroleum and marine industries. In general, HIC depends on many metallurgical factors (i.e., chemical composition, segregation, microstructure, inclusions, and microstructural defects[1,2]) that occur widely in steels used in corrosive environments in the absence of external strain. Nevertheless, HIC susceptibility can be decreased by various procedures such as control of inclusion morphology and center segregations,[3] sulfur removal, and inclusion shape modification via Ca ladle treatment,[4] heat treatment to remove the absorbed hydrogen,[5] and sensitization preventing (i.e., reducing the carbon content and adding stabilizers such as niobium or titanium[6–8]). These strategies have not been completely effective in the elimination of HIC. Therefore, a novel method based on engineering the crystallographic orientation and grain boundary characteristics was developed.[9] The mechanism of HIC at the crystal scale is described by hydrogen-enhanced decohesion (HEDE), absorption-induced dislocation emission (AIDE), and hydrogen-enhanced plasticity (HELP) theories.[10,11] HEDE is related to increasing internal pressure at trap sites as a result of the recombination of hydrogen molecules leading to crack nucleation. Next, AIDE is associated with a cleavage-like fracture in low-resistance paths to release the energy. Finally, HELP is associated with a lack of sufficient slip systems, facilitating crack growth and propagation in material.

The improving of HIC susceptibility by controlling crystallographic orientation was deduced from the fact that the lattice orientation of an individual grain and its orientation in relationship to adjacent grains play a significant role in the final mechanical properties. Blonde et al.[12] and Ghosh et al.[13] studied the relation of the lattice plane strains of grains for specific {hkl} planes oriented along the tensile direction. They showed that grains oriented along {200} planes, which are known as the least dense crystallographic planes in a body-centered cubic (BCC) lattice, are the most sensitive to applied stain. In contrast, the grains lying on the {110},

(Published online March 20, 2017)

Table I. Chemical analysis (optical emission spectroscopy) of investigated samples (in wt.%)

	C	Mn	Cr	Ni	Co	Mo	Si	P	S	Ti
Ferritic API 5L X70 steel	0.099	1.664	0.021	0.022	–	0.816	0.258	0.018	0.005	0.061
18 Ni (300) maraging steel	0.008	0.018	–	18.68	9.621	4.873	0.068	0.004	0.002	0.871
UNS 17400 martensitic stainless steel	0.019	0.822	15.677	4.225	–	–	0.302	0.022	0.016	0.166

{220}, and {211} planes provide sufficient slip systems to facilitate dislocation movement and prevent the formation of localized stress concentration by dislocation accumulation. Venegas et al.[14] reported that HIC tends to propagate along the grains oriented with {001} planes parallel to rolling plane, whereas {110} and {111} grains ({hkl}//ND, normal direction) are considered to be high-resistance crack propagation. Moreover, Szpunar et al.[15,16] documented the importance of grain boundary distributions ahead of the crack tip. They explained that low-angle boundaries (LABs) and coincidence site lattices (CSLs) are resistant to crack propagation through the formation of better lattice compliance in adjacent grains, whereas high-angle boundaries (HABs) with high stored energy provoke crack propagation.

In the current work, three different type of steels with a distinct chemical composition—American Petroleum Institute (API) steel, precipitation-hardened (PH) stainless steel, and maraging steel—were selected. The reason for the choice of these steels was their applications in industrial sectors. API steels are used as line pipes in the transportation of crude oil and gasses such as atomic hydrogen, which represent dangerous contaminants. PH stainless steels are extensively used as tube and plates in furnaces and reactors that operate at a high temperature and pressure, in a hydrogenated environment, making the operation highly critical. Maraging steel, although not extensively used in the equipment of the petroleum industry, is a strong candidate to substitute many alloys in which high strength and toughness are required. HIC susceptibility during servicing is the main restriction in developing their applications in the aggressive environment. Beside the distinct microstructure produced in each of these materials as a result of different chemical compositions, the investigated specimens are all known as having a BCC structure. Therefore, the study of the effects of crystallographic texture and boundary characteristics engineering in the matrix through the rolling process on HIC resistance was the primary objective of this work. Then, the samples subjected to electrochemical hydrogen-charging test were analyzed by electron backscattered diffraction (EBSD) examinations to investigate the effect of grain orientations and boundary types on improving HIC resistance.

EXPERIMENTAL PROCEDURES

Three different commercially available types of steels—American Petroleum Institute (API) steel, precipitation-hardened (PH) stainless steel[17] (used in a sour environment, i.e., containing water and H_2S), and maraging steel, which is used in the marine industries where it is exposed to hydrofluoric acid (HF)—were selected in this study as they are all susceptible to HIC. Table I presents the chemical compositions of the investigated steels obtained by optical emission spectrometry technique. It is notable that the low carbon content ($<0.02\%$) in these steels cannot occupy the octahedral positions in the BCC lattice. Thus, a body-centered tetragonal (BCT) martensite structure could not form and BCC structure resulted in 18 Ni (300) maraging and 17-4 PH martensitic stainless steels even under rapid quenching.[18]

To analyze the HIC resistance of commercially available as-received materials, two specimens of each material were prepared from the mid-thickness region, which is considered to be the area most susceptible to HIC, and were subjected to the electrochemical hydrogen charging test. In the electrochemical hydrogen-charging test, a 0.2-M sulfuric acid solution was used for hydrogen charging. Moreover, to prevent the formation of hydrogen bubbles on the surface of the specimen and to increase the amount of hydrogen entering the steel, 3 g/L of arsenic trioxide (As_2O_3) was added to the solution. Three samples from each steel plate were cut with dimensions of 150(RD) × 100(TD) × 10(ND) mm. Each sample was then electrochemically charged for 6 h with a constant current of 20 mA/cm^2. Finally, EBSD examination was carried out on a FEI Quanta 450 FEG scanning electron microscope (SEM) equipped with Oxford Instruments HKL Channel 5 data acquisition and analysis software. An operating voltage of 20 kV was used to optimize the diffraction patterns of the BCC martensite Kikuchi pattern.

From the literature,[19–21] it has been found that controlled warm rolling—between half of the melting point and the non-recrystallization temperature (T_{NR})—produces the favorable {111}//ND and {110}//ND crystallographic texture in ferritic steel, in which a good combination of mechanical properties and corrosion resistance is obtained. Therefore, controlled warm rolling was performed isothermally

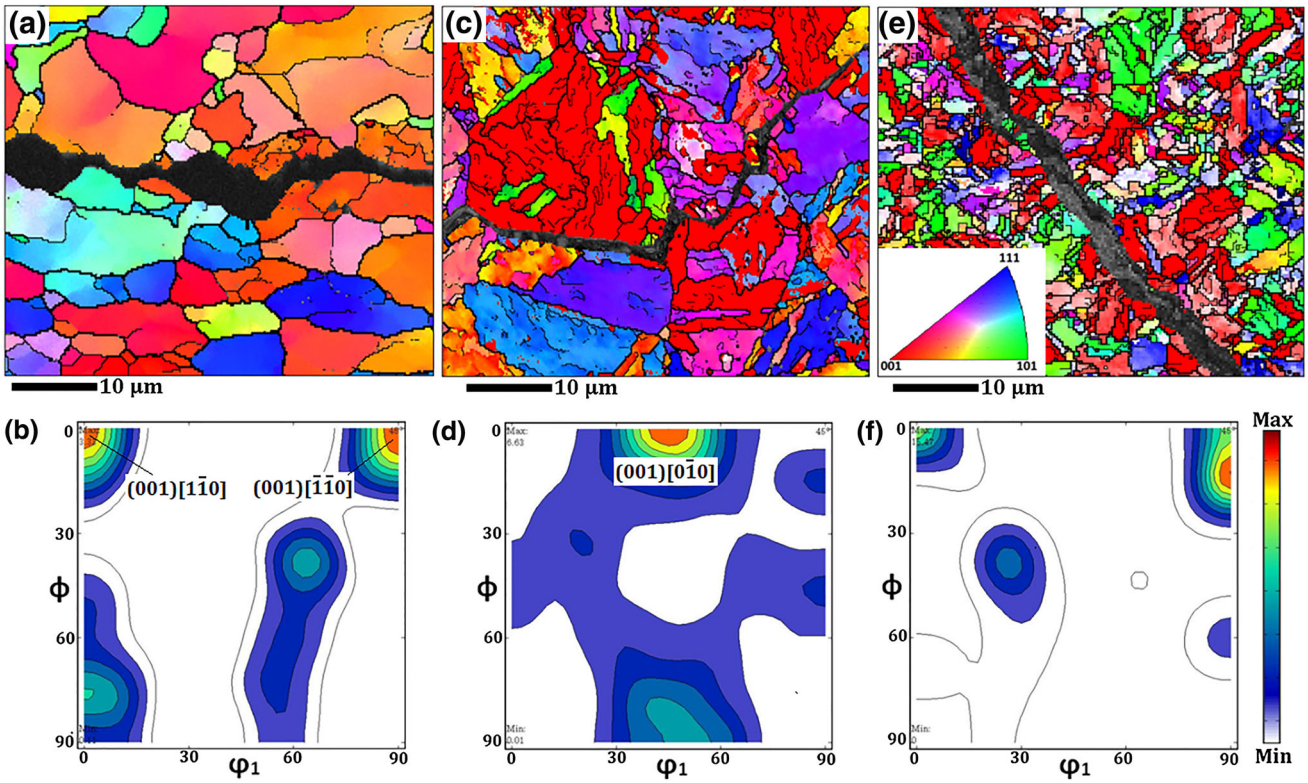

Fig. 1. IPF and related ODF in the φ_2 = 45° section: (a, b) API X70, (c, d) maraging steel, and (e, f) martensitic stainless steel.

at 850 ± 10 °C, which is low enough to prevent austenite recrystallization in the investigated steels. A Stanat model TA-315 rolling machine was used with 273 rpm rotational speed, and temperature tracking during the rolling operation was carried out by the Minolta/Land Cyclops 152 Infrared Thermometer. Rolling was conducted in three passes to reach the 75% thickness reduction to assure that a deformed texture is induced throughout the materials.

Macrotexture measurements were carried out with a Phillips X-Pert diffractometer equipped with a texture goniometer on 5 cm^2 of the sample from the rolling plane. Three incomplete pole figures, i.e., {110}, {200}, and {211}, were obtained with Co radiation in the reflection mode on a 5° grid with up to 85° sample tilt. Orientation distribution functions (ODFs) were calculated by a MTEX-free and open-source software toolbox.

RESULTS AND DISCUSSION

The normal-direction inverse pole figures (IPFs) of samples after electrochemical hydrogen charging in the vicinity of the crack propagation regions are shown in Fig. 1. It is observed that the boundaries associated with grains oriented along the {001} planes parallel to the normal direction (red color grains) are highly susceptible to crack propagation and provide easier paths for crack propagation. Moreover, in situ synchrotron x-ray diffraction analysis during tensile loading under hydrogen charging revealed that {001} crystallographic planes accumulate a much larger lattice strain in comparison with the {111} planes,[22] which can facilitate crack propagation along the {001} grains. Therefore, an increase in the proportion of the grains oriented along the {001} planes parallel in the normal direction led to greater HIC susceptibility. Although the IPF orientation map is an excellent method of presenting grain orientation, it has an unavoidable limitation in the Euler scheme.[23] To correct this limitation, the orientation distribution function (ODF) of each IPF map close to the crack path was calculated and is shown as well. The cube {001}⟨100⟩ and rotated cube {001}⟨110⟩ within around 15° of the ideal rotated cube component are found close to the crack propagation regions and are presented in Fig. 1b, d, and f. Cube and rotated cube orientations are considered to be the principal components in recrystallized austenite materials. According to Ref. 24, low-resistance cleavage paths associated with HIC propagation were found by grains with orientations within 15° of the ideal {001}ND texture fiber. Nevertheless, cube component {100}⟨011⟩, with its faces inclined at 45° along the rolling plane of the pipe wall, suffered a maximum shear stress during plastic deformation. Consequently, a cube component is more susceptible to HIC cracks.

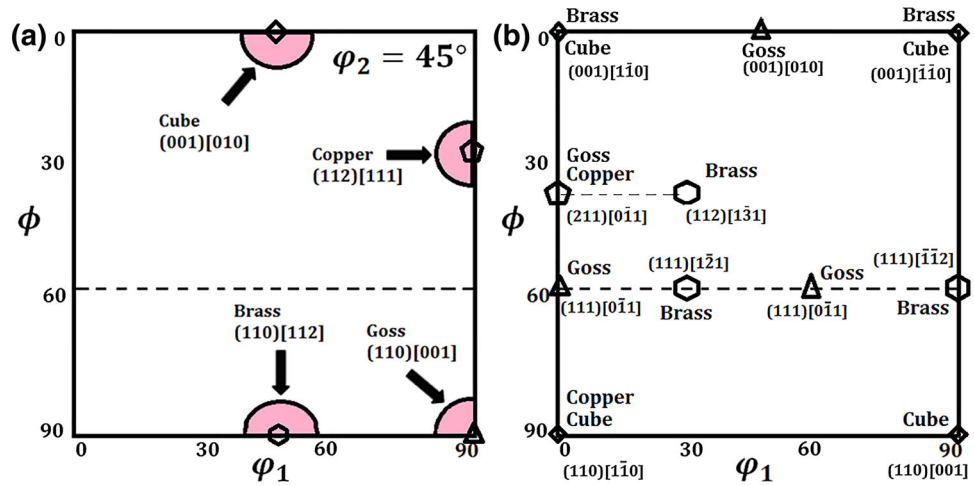

Fig. 2. ODF in the φ_2 = 45° section: (a) FCC texture components and (b) BCC texture components generated the transformation of the FCC components.[14]

When austenite is rolled in the range of the recrystallization temperature of austenite grains, the deformation textures introduced are converted by recrystallization and ferrite transformation. Cabus et al.[25] showed that the initial austenite in low-carbon steels frequently has mostly copper {112}⟨111⟩, brass {110}⟨112⟩, Goss {110}⟨001⟩, and cube {001}⟨100⟩ orientations. Then, the orientation of transformed ferrite after cooling and phase transformation can be predicted according to Kurdjumov–Sachs (K–S)[26] orientation relationships. According to the K–S orientation relationships, 24 equivalent variants of ferrite can be produced by one grain of austenite. The ideal positions of the most important BCC texture components are generated by the transformation from FCC into BCC in the φ_2 = 45° section of Euler space,[27] as shown in Fig. 2. For example, it can be seen that the FCC cube component has been transformed into the rotated cube {100}⟨011⟩, the Goss {110}⟨001⟩, and the rotated Goss {110}⟨110⟩. Ray et al.[28] and Jonas et al.[29,30] reported that the rotated cube {001}⟨110⟩ and cube {001}⟨100⟩ components are dominant and the grains oriented with {001}//ND fiber texture have the highest frequency of transformed ferrite grains. Venegas et al.[31] also reported that these texture components have undesired effects on HIC and lead to unexpected failure.

In accordance with the fact that recrystallized austenite grains followed by ferrite transformation developed the highest volume fraction of {001} grains, the deleterious effects of this texture development were observed in HIC specimens. Conversely, when pancaked austenite grains formed at a lower non-recrystallization temperature transformed into ferrite grains, the {001}//ND was only a minor component and deformation textures such as {111}//ND, {112}//ND, and {110}//ND were the principal preferred orientations. Thus, the transformation of pancaked austenite increases the number of favorable texture components and decreases the fraction of undesired {001} grains. In this respect, controlled warm rolling was performed at around 850 °C, which is low enough to prevent austenite recrystallization in the investigated materials up to a thickness reduction of 75% to assure that a deformed texture is induced throughout the materials. Figure 3 displays the ODF in the φ_2 = 45° section of Euler space of the rolled samples. The resulting texture of these rolled steels showed a deformation texture originating from a pancaked austenite rolling texture,[32–34] with characteristic components of a high number of {111}//ND and {110}//ND grains and a low number of {001} grains parallel to the normal direction. The development of {110} and {111} grains with high compact atomic planes facilitates dislocation movement along slip systems. Consequently, this prevents the formation of pile-up dislocation and local strain concentration.

Furthermore, to demonstrate the role of the controlling of crystallographic textures, the warm-rolled samples were subjected to electrochemical hydrogen charging. No cracks were observed in investigated specimens charged for 6 h, whereas after 8 h, coercive corrosion was started in susceptibility sites such as micro-precipitations, HABs, and boundaries associated with {001} grains. The results clearly showed that a significant improvement of HIC susceptibility was obtained only by controlling the crystallographic texture.

To present detailed information of the microstructural parameters such as the crystallographic orientation, boundary distributions and EBSD measurements were carried out in warm-rolled samples. Figure 4 shows the normal direction IPF maps and related ODFs. The presence of crystallographic orientations associated with {111} and {110} planes parallel to the rolling plane and deterioration of {001}//ND components produce deterioration in related ODFs. Unfortunately, the resulting ODFs

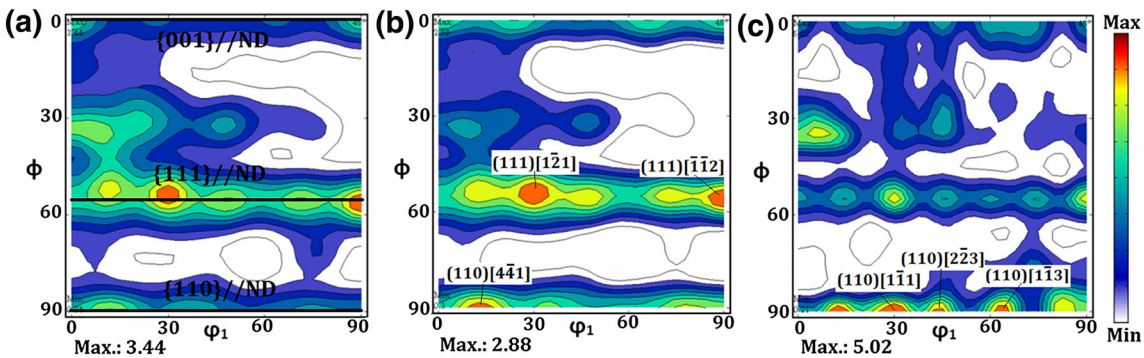

Fig. 3. ODF in the φ_2 = 45° section after warm rolling (a) API X70, (b) maraging steel, and (c) martensitic stainless steel.

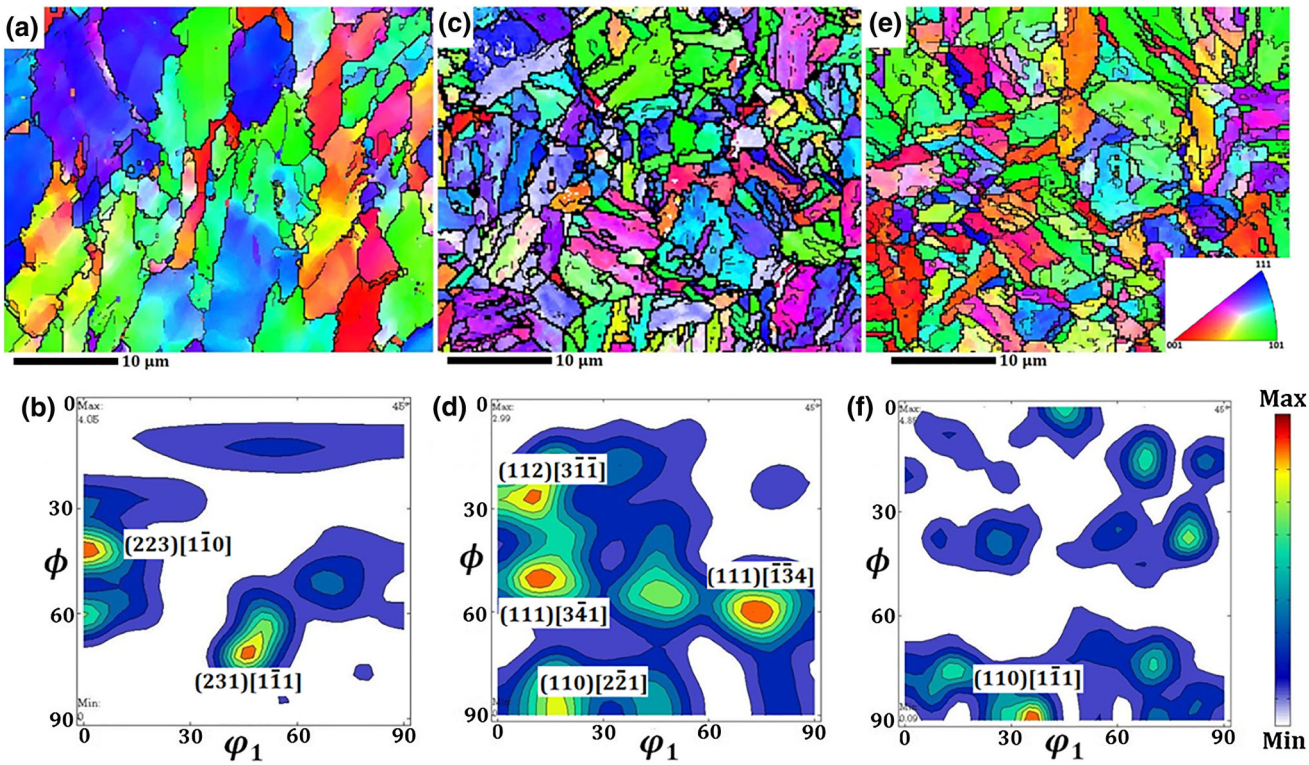

Fig. 4. IPF and related ODF of warm rolled (a, b) API X70, (c, d) maraging steel, and (e, f) martensitic stainless steels.

cannot present the grain orientation of a whole sample because of the limited number of grains that were analyzed. EBSD findings are in a good agreement with the calculated ODFs from macrotexture studies. It is worth mentioning that the development of texture lied on the atomic dense planes enhanced providing enough slip systems and facilitated dislocation motion, leading to preventing local strain concentration and improving HIC resistance.

The boundaries are described by the relative crystal lattice misorientation between the adjacent crystals. Figure 5 presents the comparison of HABs (point-to-point misorientation greater than 15°), LABs (2–15°), dislocation tangles (point-to-point misorientation less than 2°), and coincidence site lattice boundaries in all investigated samples in both conditions: as-received and warm rolled. As shown, the as-received samples demonstrated a high fraction of dislocation tangles and HABs, whereas the control warm-rolled samples had a high number of LABs and CSL boundaries. Moreover, dynamic recovery during rolling below the recrystallization temperature prevents an increase in the number of dislocation tangles by dislocation annihilation and rearrangement. Hence, the cracks can propagate easily along HABs with high stored energy; dislocation tangles also facilitate crack propagation. In addition, HABs with high dislocation density can trap more hydrogen atoms and

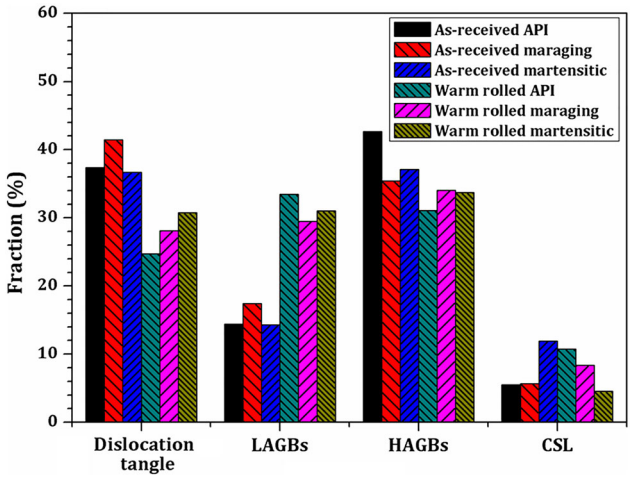

Fig. 5. Boundary distribution in as-received and warm-rolled samples.

create more internal pressure. Robertson et al.[35] produced a very interesting study correlating the hydrogen-enhanced plasticity and the hydrogen-induced fracture mechanism and pointed in its conclusions that the failure mode may be by decohesion, especially for the intergranular failure case, but the determining conditions are driven by hydrogen-enhanced plasticity.

Conversely, LABs and CSL boundaries with good lattice compliance retard crack nucleation and propagation. Also, it is notable that CSL boundaries are associated with the plane axes, and misorientations are known as crack-resistance sites.[36,37] Although the fraction of CSL boundaries increased by warm rolling, the number of CSLs in as-received UNS 17400 martensitic stainless steel was about three times higher than that in the warm-rolled condition. Thus, it is suggested that special boundaries close to low {hkl} indexing and denser packing planes in BCC lattice such as {110} and {111} are more efficient than CSLs, which lie in the {001} planes.

CONCLUSION

The effect of crystallographic texture and grain boundary distributions tailored by rolling at 850 °C in three different steels with a body-centered cube structure was investigated on HIC resistance. The XRD and EBSD techniques provided a detailed description of the behavior of individual crystal orientations and grain boundaries against HIC corrosion, and this is the most beneficial goal of the current study. The results show that increasing the fraction of LABs and CSL related to low {hkl} indexing correspond to the dense planes targeted in the grain boundary engineering to improve HIC resistance. Increasing the number of {111} and {110} grains, with the goal of minimizing the number of {001} grains and HABs, leads to a reduction in crack nucleation and propagation. Consequently, the findings demonstrated a significant improvement of HIC resistance through controlling the crystallographic texture and boundary distribution types in a BCC structure.

ACKNOWLEDGEMENTS

The authors acknowledge the Brazilian research agencies CNPq and CAPEs, the research board of the Federal University of Ceará for the financial support, and Laboratório de Caracterizacão de Materiais (LACAM) and Analytical Center (CT-INFRA/MCTI-SISNAD) for the provision of research facilities of this work.

REFERENCES

1. M. Masoumi, C.C. Silva, and H.F.G. Abreu, *Corros. Sci.* 111, 121 (2016).
2. S.S. Nayak, R.D.K. Misra, J. Hartmann, F. Siciliano, and J.M. Gray, *Mater. Sci. Eng., A* 494, 456 (2008).
3. H.B. Xue and Y.F. Cheng, *Corros. Sci.* 53, 1201 (2011).
4. L.F. Zhang, *J. Iron. Steel Res. Int.* 13, 1 (2006).
5. T. Hyodo, M. Iino, A. Ikeda, M. Kimura, and M. Shimizu, *Corros. Sci.* 27, 10 (1987).
6. G. Pantazopoulos and A. Vazdirvanidis, *Eng. Fail. Anal.* 16, 1623 (2009).
7. G. Bai, S. Lu, D. Li, and Y. Li, *Corros. Sci.* 90, 347 (2015).
8. K.H. Lo, D. Zeng, and C.T. Kwok, *Mater. Sci. Eng., A* 528, 1003 (2011).
9. V. Venegas, F. Caleyo, J.L. González, T. Baudin, J.M. Hallen, and R. Penelle, *Scr. Mater.* 52, 147 (2005).
10. M.A. Mohtadi-Bonab, M.M. Eskandari, K.M.M. Rahman, R. Ouellet, and J.A. Szpunar, *Int. J. Hydrogen Energy* 41, 4185 (2016).
11. J. Moon, J. Choi, S.K. Han, S. Huh, S.J. Kim, C.H. Lee, and T.H. Lee, *Mater. Sci. Eng., A* 652, 120 (2016).
12. R. Blondé, E. Jimenez-Melero, L. Zhao, J.P. Wright, E. Brück, S. van der Zwaag, and N.H. Dijk, *Acta Mater.* 60, 565 (2012).
13. A. Ghosh, S. Kundu, and D. Chakrabarti, *Scr. Mater.* 81, 8 (2014).
14. V. Venegas, F. Caleyo, T. Baudin, J.H. Espina-Hernández, and J.M. Hallen, *Corros. Sci.* 53, 12 (2011).
15. J.A. Szpunar, M.A. Mohtadi-Bonab, and M. Eskandari, *Mater. Sci. Eng., A* 620, 97 (2015).
16. J.A. Szpunar, Y. Hayakawa, and M. Muraki, *Acta Mater.* 46, 1063 (1998).
17. W.C. Chiang, C.C. Pu, B.L. Yu, and J.K. Wu, *Mater. Lett.* 57, 2485 (2003).
18. U.K. Viswanathan, G.K. Dey, and M.K. Asundi, *Metall. Trans. A* 24A, 2429 (1993).
19. R. Unnikrishnan, A. Kumar, R.K. Khatirkar, S.K. Shekhawat, and S.G. Sapate, *Mater. Chem. Phys.* 183, 339 (2016).
20. F. Gao, Z. Liu, H. Liu, and G. Wang, *Mater. Charact.* 75, 95 (2013).
21. J. Henry and S.A. Maloy, *Structural Materials for Generation IV Nuclear Reactors*, ed. P. Yvon (Elsevier, 2017), pp. 329–355.
22. D.M. Collins, M. Mostafavi, R.E. Todd, T. Connolley, and A.J. Wilkinson, *Acta Mater.* 90, 46 (2015).
23. P.X. Gao and Z.L. Wang, *Scanning Microsc. Nanotechnol.* 41, 384 (2007).
24. V. Venegas, F. Caleyo, M. Hallen, T. Baudin, and R. Penelle, *Metall. Mater. Trans. A* 38, 1022 (2007).
25. C. Cabus, H. Réglé, and B. Bacroix, *Mater. Charact.* 58, 332 (2007).
26. G. Kurdjumow and G. Sachs, *Z. Phys.* 64, 325 (1930).
27. R. Winston Revie, *Oil and Gas Pipelines: Integrity and Safety Handbook* (Hoboken: Wiley, 2015), pp. 157–186.

28. R.K. Ray, M.P. Butrón-Guillén, J.J. Jonas, and G.E. Ruddle, *ISIJ Int.* 32, 203 (1992).
29. J.J. Jonas, R. Petrov, and L. Kestens, *Proceedings of the 2nd Baosteel Biennial Academic Conference*, 1, 319 (2006).
30. R.H. Petrov, J.J. Jonas, and L.A.I. Kestens, *Oil and Gas Pipelines: Integrity and Safety Handbook* (Hoboken: Wiley, 2007).
31. V. Venegas, F. Caleyo, T. Baudin, J.H. Espina-Hernández, and J.M. Hallen, *Corros. Sci.* 53, 4204 (2011).
32. A.A. Gazder, M.S. Araiza, J.J. Jonas, and E.V. Pereloma, *Acta Mater.* 59, 4847 (2011).
33. M. Masoumi, I.F. Barros, L.F.G. Herculano, H.L.F. Coelho, and H.F.G. Abreu, *Mater. Charact.* 20, 203 (2016).
34. L. Storojeva, D. Ponge, R. Kaspar, and D. Raabe, *Acta Mater.* 52, 2209 (2004).
35. I.M. Robertson, P. Sofronis, A. Nagao, M.L. Martin, S. Wang, D.W. Gross, and K.E. Nygren, *Metall. Mater. Trans. A* 46A, 2323 (2015).
36. S. Jothi, T.N. Croft, L. Wright, A. Turnbull, and S.G.R. Brown, *Int. J. Hydrogen Energy* 40, 15105 (2015).
37. M. Masoumi, L.F.G. Herculano, A.A. Almeida, M. Béreš, and H.F.G. Abreu, *JOM* 68, 401 (2016).